Geology, 2015, doi: 10.1130/G36983.1
Accepted, Pre-Copy Edit version

Carbon sequestration on Mars

Christopher S. Edwards[1*] and Bethany L. Ehlmann[1,2]

[1]*California Institute of Technology,1200 E. California Boulevard, MC 150-21, Pasadena, California 91125, USA*

[2]*Jet Propulsion Laboratory/ California Institute of Technology, Pasadena, California 91109, USA*

*Current address: U.S. Geological Survey Astrogeology Science Center, 2255 N. Gemini Road, Flagstaff, Arizona 86001, USA.

ABSTRACT

On Earth, carbon sequestration in geologic units plays an important role in the carbon cycle, scrubbing CO_2 from the atmosphere for long-term storage. While identified in low abundances within the dust and soils, at <1 wt% in select meteorites, and in limited outcrops, no massive carbonate rock reservoir on Mars has been identified to date. Here, we investigate the largest exposed carbonate-bearing rock unit, the Nili Fossae plains, combining spectral, thermophysical and morphological analyses to evaluate the timing and carbon sequestration potential of rocks on Mars. We find the olivine-enriched (~20%–25%) basalts have been altered, by low-temperature, in-situ carbonation processes, to at most ~20% Fe-Mg carbonate, thus limiting carbon sequestration in the Nili Fossae region to ~0.25–12 mbar of CO_2 during the late Noachian/early Hesperian, before or concurrent with valley network formation. While large compared to modern-day CO_2 reservoirs, the lack of additional, comparable-sized post-Late Noachian carbonate-bearing deposits on Mars indicates ineffective carbon sequestration in rock units over the past ~3.7 Ga. This implies a thin atmosphere ($\lesssim$500 mbar) during valley network formation, extensive post-Noachian atmospheric loss to space or diffuse, deep sequestration by a yet-to-be understood process. In stark contrast to Earth's biologically mediated crust:atmosphere carbon reservoir ratio of ~10^4–10^5, Mars' ratio is a mere 10–10^3, even if buried pre-Noachian crust holds multiple bars.

Geology, 2015, doi: 10.1130/G36983.1
Accepted, Pre-Copy Edit version

INTRODUCTION

Martian carbonates have been observed telescopically, from orbit (e.g., Bandfield et al., 2003; Ehlmann et al., 2008; Michalski and Niles, 2010), in situ (e.g., Boynton et al., 2009; Morris et al., 2010) and in Martian meteorites; however, a long-postulated geologic reservoir that accounts for proposed thinning of a multi-bar early Mars atmosphere by CO_2 sequestration (Booth and Kieffer, 1978; Pollack et al., 1987) has not yet been identified (Niles et al., 2013). One striking aspect of the Martian geologic record is the presence of valley networks and open basin lakes last active around the Noachian/Hesperian boundary, at ca. 3.5 Ga (Fassett and Head, 2008). If surface waters were supported by a thicker atmosphere (Hynek et al., 2010), hundreds of millibars to bars of CO_2 would need to be lost to space during the Hesperian/Amazonian, inconsistent with models (e.g., Lammer et al., 2013). Was this late CO_2 sequestered in the Martian crust? We consider the role of diffuse and localized CO_2 sequestration and constrain the timing/implications for late Noachian atmospheric conditions via examination of the age and composition of the largest contiguous exposure of carbonate-bearing rock on Mars, the Nili Fossae carbonate plains (21.5°N, 78.5°E; Ehlmann et al., 2008). Morphological, spectral and thermophysical data sets, Thermal Emission Spectrometer (TES), Compact Reconnaissance Imaging Spectrometer for Mars (CRISM), Thermal Emission Imaging System (THEMIS), Context Imager (CTX) and High Resolution Imaging Science Experiment (HiRISE) are considered in the context of past atmospheric drawdown.

MINERAL MAPPING AND ABUNDANCES

At a scale of kilometers, we map two distinct TES spectral units using the carbonate decomposition product/carbonate index (Fig. 1; Table DR1; Glotch and

Rogers, 2013). Basaltic terrains (TES^{C}) have low carbonate (~10%), low olivine (~4%), and elevated feldspar/pyroxene abundances similar to Syrtis Major (Rogers and Christensen, 2007). In contrast, TES$^{A\&B}$ have elevated Fe-Mg carbonate (~15%), ~20% olivine (~Fo60–70; Hamilton and Christensen, 2005), and comparable pyroxene but substantially less feldspar. Carbonate is close to the detection limit for TES^{C} and TES$^{A\&B}$; however, TES$^{A\&B}$ spectral model fits (specifically the ~350 cm^{-1} feature) are improved by the additional ~5% carbonate and are not well matched by increases in other mafic minerals with absorptions at these wavelengths. High-Si phases are elevated (~20%) in all TES spectra, likely evidence of the aqueous alteration prevalent in the region (Mangold et al., 2007; Rogers and Christensen, 2007). Carbonate content of ~5% is a minimum as the TES footprints are a combination of carbonate and non-carbonate bearing materials observed at finer-scales (CRISM, HiRISE; Figs. 2 and 3).

Five distinct CRISM spectral units are identified (Fig. 2), correlated with morphology (Fig. 3): (1) low-albedo, olivine-bearing basaltic bedrock; (2) olivine-enriched basaltic sands; (3) olivine/carbonate-bearing basaltic bedrock; (4) a basaltic capping unit; and (5) an Fe-Mg smectite-bearing Noachian basement (not investigated here, see Ehlmann et al., 2009; Mustard et al., 2009). Spectra from morphological units (1–3) have similar spectral shapes around ~1 µm (Fig. 2b), distinct from (4) and consistent with intermediate Fo$_{\#}$ and/or large grain size olivine.

Hapke modeling of single scattering albedo (SSA) spectra extracted from DISORT-processed CRISM data yields mineral abundances and grain sizes (Table DR2; Fig. 2). The carbonate-bearing unit (3) has ~15% (1 mm grain size) carbonate in an olivine-enriched (~25%, ~1 mm) basalt (~60%, ~1 mm), with minimal Fe-Mg smectite

(<2%). Other olivine-bearing units (1–2) have ~20%–30% olivine and are coarse-grained (~1 mm) with ~60% basalt and negligible carbonate. The basaltic cap unit (4) is distinct, composed mostly of a finer-grained (~400 μm) basaltic material with little olivine or smectite. A second modeling approach with scene-derived olivine bedrock SSA (unit 3) and lab-derived carbonate SSA indicates ~5% carbonate, using the observed depth of the 2.5 μm absorption (the most unique indicator of carbonate; Ehlmann et al., 2008) (Fig DR1).

THEMIS band 7 band depth is correlated with the CRISM OLINDEX2 (olivine index). THEMIS ratio data show a downturn in bands 1/2 correlated with and coincident with locations where CRISM shows the strongest band depths at 2.3 and 2.5 μm (Fig. 4; Fig. DR2). An olivine-carbonate mixture and olivine spectra are good matches for the ratio spectra extracted from spatially coherent THEMIS data (Fig. 4b).

MORPHOLOGY

Carbonate abundance is anti-correlated with the presence of the olivine-bearing sand cover (Fig. 2c). The carbonate-bearing unit is highly fractured and light-toned with darker, fracture-filling materials (likely sand; Fig. 3b). The carbonate-poor/olivine-bearing outcrops exhibit a rough and pitted texture and typically lie stratigraphically above the olivine-/carbonate-bearing unit with a seemingly conformable contact (Fig. 3b). Notably, the carbonate-poor/olivine-bearing rock is morphologically distinct from the capping unit, which has a massive appearance (Fig. 3).

PHYSICAL PROPERTIES

Regional thermal inertia (TI) ranges from ~250 to 600 J m^{-2} K^{-1} $s^{-1/2}$ (hereafter SI), corresponding to grain sizes from fine regolith (~300 μm) to weakly

Geology, 2015, doi: 10.1130/G36983.1
Accepted, Pre-Copy Edit version

consolidated/heavily altered bedrock (>1 mm), inconsistent with crystalline Martian volcanics (>1200 SI in THEMIS; Edwards et al., 2009). Surface materials (e.g., aeolian bedforms, dust) can reduce derived TI, but many clean exposures are observed at HiRISE scales.

The thermophysical and compositional characteristics show distinct groupings. The olivine-/carbonate-bearing materials typically have TI of ~400–500 SI (Fig. 2; Fig. DR3), and the ~10% higher TI in olivine-bearing/carbonate-poor materials can be explained solely by their lower albedos below the spatial scale used in TI modeling (Fergason et al., 2006a). Olivine-basalt sands have TI of ~350 SI ($\gtrsim$1 mm grains), while the low-olivine capping unit has TI of 250–300 SI (~300–700 μm grains; Fig. 2d; Fig. DR3a; Piqueux and Christensen, 2011), consistent with CRISM-derived grain sizes.

GEOLOGIC HISTORY AND ENVIRONMENTAL IMPLICATIONS

Olivine abundances (20%–25%) suggest the olivine-bearing basalts in Nili Fossae are likely picritic, resembling the Adirondack rock class from Gusev (McSween et al., 2006). Previously, the olivine-bearing materials were interpreted as olivine-enriched basalt flows (Hamilton and Christensen, 2005) predating the Isidis impact or cumulates settled from the Isidis-derived impact melt sheet (Mustard et al., 2009). However, the low TI of these unmantled olivine-enriched units is inconsistent with crystalline igneous rocks (e.g., Adirondack) but is similar to that of the clastic olivine/-carbonate-bearing rocks (Comanche/Algonquin classes, ~550 SI) observed in the Columbia Hills (Fig. 1b; Fergason et al., 2006b; Ruff et al., 2014) or highly fractured materials. The basaltic capping unit, while forming significant topographic highs, has the lowest TI (~300 SI).

Its distinct composition, morphology and thermophysical properties suggest that it may be an eroded ash deposit (e.g., Bandfield et al., 2013).

The olivine-enriched and olivine-/carbonate-enriched units are likely the same original lithology, given their similar compositions (except for Mg-Fe carbonate), morphology and TI. Their low TI suggests a clastic rock or pervasive fracturing at cm-scale in a crystalline igneous rock. Given the fractures observed (advantageous for fluids to migrate more easily) and mineral assemblages/abundances, we find the likely scenario for the formation of the Nili Fossae carbonate plains is low-temperature, in situ carbonation (van Berk and Fu, 2011), akin to the Samail ophiolite in Oman (Kelemen and Matter, 2008) or in-place serpentinization reactions. Variability of fractures/pore-space in the precursor rock or limited groundwater percolation may produce the spatial variability of carbonate-bearing outcrops, leaving some regions largely unaltered.

Of critical importance is the timing of carbonation and atmospheric CO_2 sequestration in the Nili Fossae and in other potential reservoirs. Sequestration in Nili Fossae must have occurred after emplacement of the olivine-rich precursor (syn- or post-Isidis formation, i.e., early/middle Noachian; Hamilton and Christensen, 2005; Mustard et al., 2009). The carbonate-bearing units are incised by valley networks and overlain by the Hesperian Syrtis Major unit, indicating carbonation prior to or contemporaneous with valley network formation. This important local timing constraint can be extended globally, as >50% of the Mars surface is comprised of Noachian and Hesperian terrains of similar age or younger than Isidis (Tanaka et al., 2014). The lack of additional late Noachian and younger carbonate-bearing units is not likely a sampling bias as a host of other secondary minerals are observed (Ehlmann and Edwards, 2014).

CARBONATE ABUNDANCE, EXTENT AND CO_2 SEQUESTRATION POTENTIAL

TES and CRISM locations with elevated carbonate spatially correlate, and quantitative modeling agrees on total carbonate (~5%–15%) and relative differences in carbonate abundance (~5%–15%). In the inverse model, the diagnostic 2.5-µm absorption is overmodeled (Fig. 2b), favoring the ~5% CRISM-derived carbonate abundance from forward modeling (Fig. S1). Checkerboard mixing of olivine-basaltic sands at sub-CRISM pixel scales lowers the apparent carbonate abundance; though HiRISE 25 cm/pixel data suggest >75% of the surface is clean. By coupling HiRISE to TES/CRISM abundances, our work indicates ~20% carbonate is a likely maximum for Nili Fossae carbonate plains bedrock. The areal extent of the unit is constrained using only carbonate-bearing outcrop exposures (~6800 km^2) or the entire extent of the regional Nili Fossae olivine outcrops (300,000 km^2) that are variably buried by Syrtis lavas. Depth is constrained by a 6-km-diameter impact crater excavating ~500 m and beneath the carbonate (21.35°N, 78.80°E), previous estimates for the thickness of the olivine-bearing unit (Mustard et al., 2009), and the typical depth of in situ carbonation (≲200 m; van Berk and Fu, 2011). Thus, the Nili Fossae carbonate plains unit likely sequestered ~0.25–12 mbars of atmospheric CO_2 (~4×10^{-4} mbar of CO_2 per km^3 of $MgCO_3$).

The CO_2 sequestered in the Nili Fossae is significant relative to the current ~6 mbar atmosphere, CO_2 within the south polar cap (5 mbar; Phillips et al., 2011), and that sequestered in the ubiquitous Martian dust (~1 mbar for ~5% abundance, ~1 m thick global layer of 40% porosity; Bandfield et al., 2003). However, it is small relative to the hundreds of millibars to bars of CO_2 suggested to sustain surface waters during late

Noachian/early Hesperian valley network formation. If carbon sequestration occurred by carbonate mineralization and ≳500 mbar late-Noachian atmosphere was removed, either post-Noachian carbonate formation is more volumetrically widespread but diffuse than has been observed in landed missions and meteorites or >35 "hidden" Nili Fossae-scale post-Noachian carbonate-bearing rock deposits remain to be discovered.

While orbital remote sensing could miss small-scale deposits (e.g., Ruff et al., 2014), given the mineralogical discrimination and spatial coverage, it is unlikely that many significant reservoirs of Nili Fossae-scale and age (or younger) have been overlooked. Remote sensing data cannot exclude early- or pre-Noachian formation of carbonate bearing rocks (e.g., Michalski and Niles, 2010; Niles et al., 2013, and references therein) as these early- and pre-Noachian are deeply buried, exposed over <10% of the surface (Tanaka et al., 2014) and tapped only infrequently by impact craters. However, if an early-/pre-Noachian episode of carbon sequestration occurred, it pre-dates formation of Mars' valley networks and hence cannot explain removal of a thick atmosphere that may have enabled precipitation at that time.

Destruction of carbonates by acid waters cannot resolve the paradox of the missing carbon reservoir because dissolution would release CO_2 back into the atmosphere, i.e., a recycling resulting in no net carbon sequestration. Post Noachian deep-diffuse alteration could, however, be undetectable by remote sensing. For example, the Nakhlites and ALH84001 contain trace carbonates. Martian missions investigating equatorial geologic units have found carbonate at <2% in rocks and soils (e.g., Leshin et al., 2013), and the Phoenix lander found soil carbonates at ~5% (Boynton et al., 2009). To sequester ~500 mbar of atmospheric $CO_{2,}$ the crust would have to be altered at an average of 1 wt% to a depth of ~1 km. Sequestering carbon this deep in the crust is challenging; open hydrologic systems do not typically support alteration to great depths (≲100s of meters; van Berk and Fu, 2011) because atmospherically derived CO_2 in fluids is exhausted by mineralization, ultimately limiting carbon sequestration potential from deep, diffuse processes.

Modern Martian carbon sequestration may be prevented in most locations by either aridity, acidity, or sulfurous gases that inhibit carbonate formation (Halevy and Schrag, 2009). Either an efficient water-driven “pumping” of CO_2 down into the subsurface for deep diffuse carbon sequestration or vigorous, post-Noachian atmospheric escape to space would be required to remove a late Noachian hundreds of millibars to multi-bar CO_2 atmosphere. These high escape rates later in Mars history are not expected (Lammer et al., 2013), but the MAVEN mission will lead to an improved quantification of average loss rates. Possibly most likely, the pCO_2 of the post-Noachian atmosphere was simply low, even during the time of valley network formation. If this hypothesis is correct, the isotopic record of CO_2 should be consistent with loss predominantly to the atmosphere over time and no major crustal carbon sequestration since the early Noachian. Notably, even if multiple bars of sequestration are assumed for buried pre-Noachian units, the Martian rock reservoir contains only $10–10^3$ times the carbon in the atmosphere, in stark contrast to the $\sim10^4–10^5$ ratio for Earth, a consequence of effective, biologically driven carbon sequestration (Ronov and Yaroshevsky, 1969). Continued evaluation of carbonate in Martian meteorites and in situ analysis of chemistry, mineralogy and isotopic composition of carbonate-bearing rocks will generate new data to determine the long-term evolution of carbon geochemical cycling on Mars.

ACKNOWLEDGMENTS

We thank R.E. Arvidson for providing the CRISM DISORT processed image, A.D. Rogers the Syrtis-type TES spectra, and S. Piqueux for helpful discussions. T.D. Glotch, P. D. Niles, and an anonymous reviewer provided helpful formal reviews. A Mars Exploration Program Future Landing Sites grant administered by the Jet Propulsion Laboratory provided partial support for Edwards and Ehlmann to conduct this analysis.

Geology, 2015, doi: 10.1130/G36983.1
Accepted, Pre-Copy Edit version

REFERENCES CITED

Bandfield, J.L., Edwards, C.S., Montgomery, D.R., and Brand, B.D., 2013, The dual nature of the martian crust: Young lavas and old clastic materials: Icarus, v. 222, p. 188–199, doi:10.1016/j.icarus.2012.10.023.

Bandfield, J.L., Glotch, T.D., and Christensen, P.R., 2003, Spectroscopic identification of carbonates in the Martian dust: Science, v. 301, p. 1084, doi:10.1126/science.1088054.

Booth, M.C., and Kieffer, H.H., 1978, Carbonate formation in Mars-like environments: Journal of Geophysical Research, v. 83, B4, p. 1809–1815, doi:10.1029/JB083iB04p01809.

Boynton, W.V., et al., 2009, Evidence for calcium carbonate at the Mars Phoenix landing site: Science, v. 325, p. 61–64, doi:10.1126/science.1172768.

Edwards, C.S., Bandfield, J.L.,Christensen, P.R., and Fergason, R.L., 2009, Global distribution of bedrock exposures on Mars using THEMIS high-resolution thermal inertia: Journal of Geophysical Research, v. 114, E11001, doi:10.1029/2009JE003363.

Ehlmann, B.L., and Edwards, C.S., 2014, Mineralogy of the Martian surface: Annual Review of Earth and Planetary Sciences, v. 42, np. 291–315, doi:10.1146/annurev-earth-060313-055024.

Ehlmann, B.L., et al., 2008, Orbital identification of carbonate-bearing rocks on Mars: Science, v. 322, p. 1828, doi:10.1126/science.1164759.

Ehlmann, B.L., et al., 2009, Identification of hydrated silicate minerals on Mars using MRO-CRISM: Geologic context near Nili Fossae and implications for aqueous alteration: Journal of Geophysical Research, v. 114, E00D08, doi:10.1029/2009JE003339.

Fassett, C.I., and Head, J.W., 2008, The timing of martian valley network activity: Constraints from buffered crater counting: Icarus, v. 195, p. 61–89, doi:10.1016/j.icarus.2007.12.009.

Fergason, R.L., Christensen, P.R., and Kieffer, H.H., 2006a, High resolution thermal inertia derived from THEMIS: Thermal model and applications: Journal of Geophysical Research, v. 111, E12004, doi:10.1029/2006JE002735.

Fergason, R.L., Christensen, P.R., Bell, J.F., III, Golombek, M.P., Herkenhoff, K.E., and Kieffer, H.H., 2006b, Physical properties of the Mars Exploration Rover landing sites as inferred from Mini-TES-derived thermal inertia: Journal of Geophysical Research, v. 111, E02S21, doi:10.1029/2005JE002583.

Glotch, T.D., and Rogers, A.D., 2013, Evidence for magma-carbonate interaction beneath Syrtis Major, Mars: Journal of Geophysical Research, v. 118, p. 126–137.

Halevy, I., and Schrag, D.P., 2009, Sulfur dioxide inhibits calcium carbonate precipitation: Implications for early Mars and Earth: Geophysical Research Letters, v. 36, L23201, doi:10.1029/2009GL040792.

Hamilton, V.E., and Christensen, P.R., 2005, Evidence for extensive olivine-rich bedrock in Nili Fossae, Mars: Geology, v. 33, p. 433–436, doi:10.1130/G21258.1.

Hynek, B.M., Beach, M., and Hoke, M.R.T., 2010, Updated global map of Martian valley networks and implications for climate and hydrologic processes: Journal of Geophysical Research, v. 115, E09008, doi:10.1029/2009JE003548.

Kelemen, P.B., and Matter, J., 2008, In situ carbonation of peridotite for CO_2 storage: Proceedings of the National Academy of Sciences of the United States of America, v. 105, p. 17295–17300, doi:10.1073/pnas.0805794105.

Lammer, H., et al., 2013, Outgassing history and escape of the martian atmosphere and water inventory: Space Science Reviews, v. 174, p. 113–154, doi:10.1007/s11214-012-9943-8.

Leshin, L.A., et al., 2013, Volatile, isotope, and organic analysis of martian fines with the Mars Curiosity rover: Science, v. 341, doi:10.1126/science.1238937.

Mangold, N., et al., 2007, Mineralogy of the Nili Fossae region with OMEGA/Mars Express data: 2. Aqueous alteration of the crust: Journal of Geophysical Research, v. 112, E08S04, doi:10.1029/2006JE002835.

McSween, H.Y., et al., 2006, Characterization and petrologic interpretation of olivine-rich basalts at Gusev Crater, Mars: Journal of Geophysical Research, v. 111, E02S10, doi:10.1029/2005JE002477.

Michalski, J.R., and Niles, P.B., 2010, Deep crustal carbonate rocks exposed by meteor impact on Mars: Nature Geoscience, v. 3, p. 751–755, doi:10.1038/ngeo971.

Morris, R.V., et al., 2010, Identification of carbonate-rich outcrops on Mars by the Spirit Rover: Science, v. 329, p. 421–424, doi:10.1126/science.1189667.

Mustard, J.F., et al., 2009, Composition, morphology, and stratigraphy of Noachian crust around the Isidis basin: Journal of Geophysical Research, v. 114, E00D12, doi:10.1029/2009JE003349.

Niles, P.B., et al., 2013, Geochemistry of carbonates on Mars: Implications for Climate history and nature of aqueous environments: Space Science Reviews, v. 174, p. 301–328, doi:10.1007/s11214-012-9940-y.

Phillips, R.J., et al., 2011, Massive CO_2 Ice deposits sequestered in the south polar layered deposits of Mars: Science, v. 332, p. 838–841, doi:10.1126/science.1203091.

Piqueux, S., and Christensen, P.R., 2011, Temperature-dependent thermal inertia of homogeneous Martian regolith: Journal of Geophysical Research, v. 116, E07004, doi:10.1029/2011JE003805.

Pollack, J.B., et al., 1987, The case for a wet, warm climate on early Mars: Icarus, v. 71, p. 203–224, doi:10.1016/0019-1035(87)90147-3.

Rogers, A.D., and Christensen, P.R., 2007, Surface mineralogy of martian low-albedo regions from MGS TES data: Implications for crustal evolution and surface alteration: Journal of Geophysical Research, v. 112, E01003, doi:10.1029/2006JE002727.

Ronov, A.B., and Yaroshevsky, A.A., 1969, Chemical Composition of the Earth's Crust, *in* Hart, P.J., ed., The Earth's Crust and Upper Mantle: Washington, D.C., American Geophysical Union, p. 37–57.

Ruff, S.W., Niles, P.B., Alfano, F., and Clarke, A.B., 2014, Evidence for a Noachian-aged ephemeral lake in Gusev crater, Mars: Geology, v. 42, p. 359–362, doi:10.1130/G35508.1.

Tanaka, K.L., et al., 2014, Geologic Map of Mars: U.S. Geologic Survey Scientific Investigations Map 3292, scale 1:20,000,000, with 43 p. pamphlet.

van Berk, W., and Fu, Y., 2011, Reproducing hydrogeochemical conditions triggering the formation of carbonate and phyllosilicate alteration mineral assemblages on Mars (Nili Fossae region): Journal of Geophysical Research, v. 116, E10006, doi:10.1029/2011JE003886.

FIGURE CAPTIONS

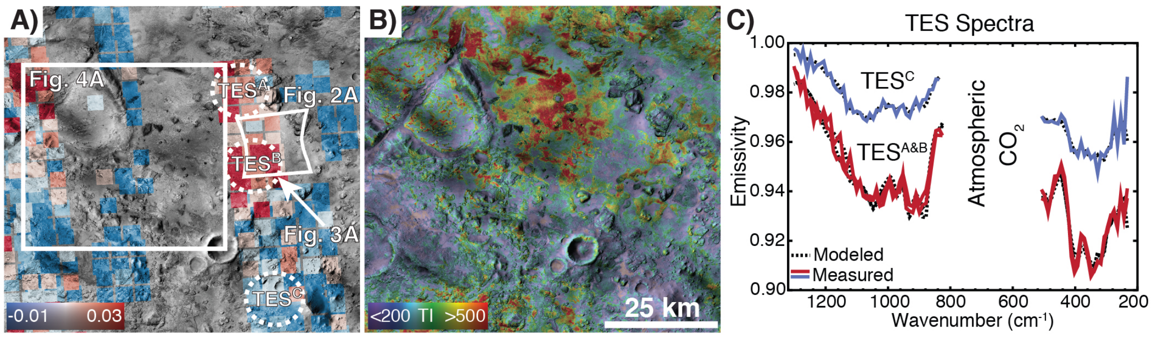

Figure 1. A: TES carbonate decomposition product/carbonate index (Glotch and Rogers, 2013) over a CTX mosaic (6 m/px, ~21.5°N, 78.5°E) highlights locations with carbonate which are of moderate TI in (B) THEMIS TI over a CTX mosaic. C: TES spectral observations (OCK 3358) corresponding to the locations in A. TES^{C} is consistent with typical Syrtis Major compositions. $TES^{A\&B}$ have increases in both olivine (~23%) and Fe-Mg carbonate (~15%) over TES^{C}. Abundances are detailed in Table DR1 and the endmember library in Table DR3 (see footnote 1).

Geology, 2015, doi: 10.1130/G36983.1
Accepted, Pre-Copy Edit version

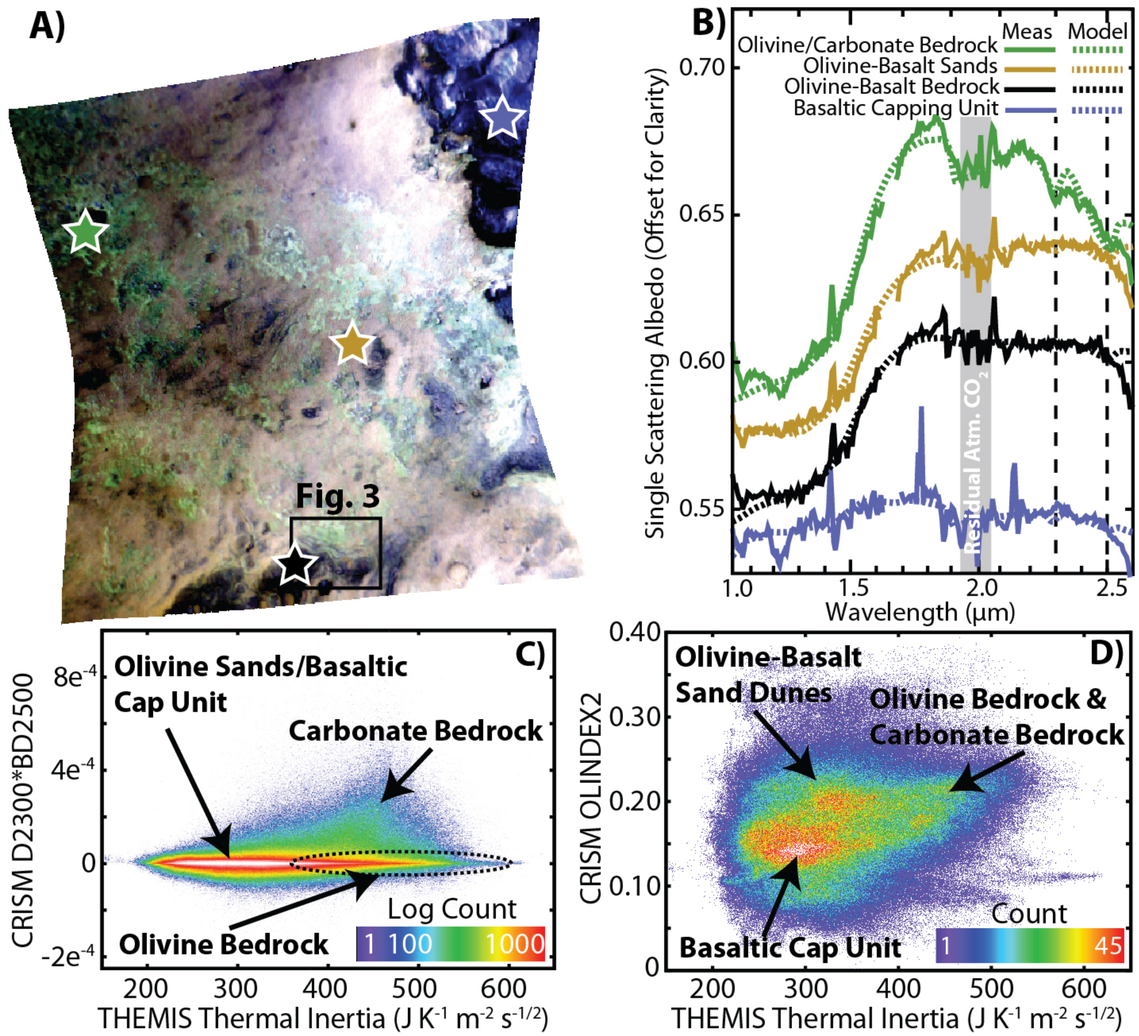

Figure 2. A: CRISM (FRT000C968) SSA image (RGB; 2.38, 1.80, 1.15 µm), where green indicates carbonate-bearing material, brown/yellow correlates with olivine-basalt sands and purple is typical of the basaltic capping unit and dark-toned olivine-enriched units. B: SSA spectra and forward Hakpe model fits from the locations identified in A. Each spectrum corresponds to a unique morphology highlighted in Fig. 3. C,D: CRISM band indices THEMIS TI for the region in Fig. 1.

Geology, 2015, doi: 10.1130/G36983.1
Accepted, Pre-Copy Edit version

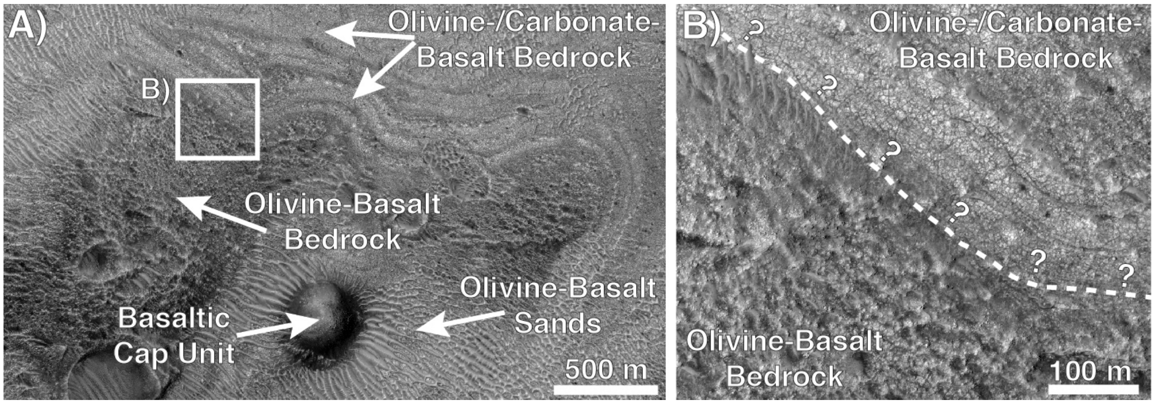

Figure 3. HiRISE image (PSP_010351_2020). A: Contact between the basaltic cap unit and underlying bedrock, plus olivine-basalt sands atop the olivine-/carbonate-enriched bedrock. B: Potential contact between the carbonate-bearing bedrock and the overlying olivine-basalt bedrock.

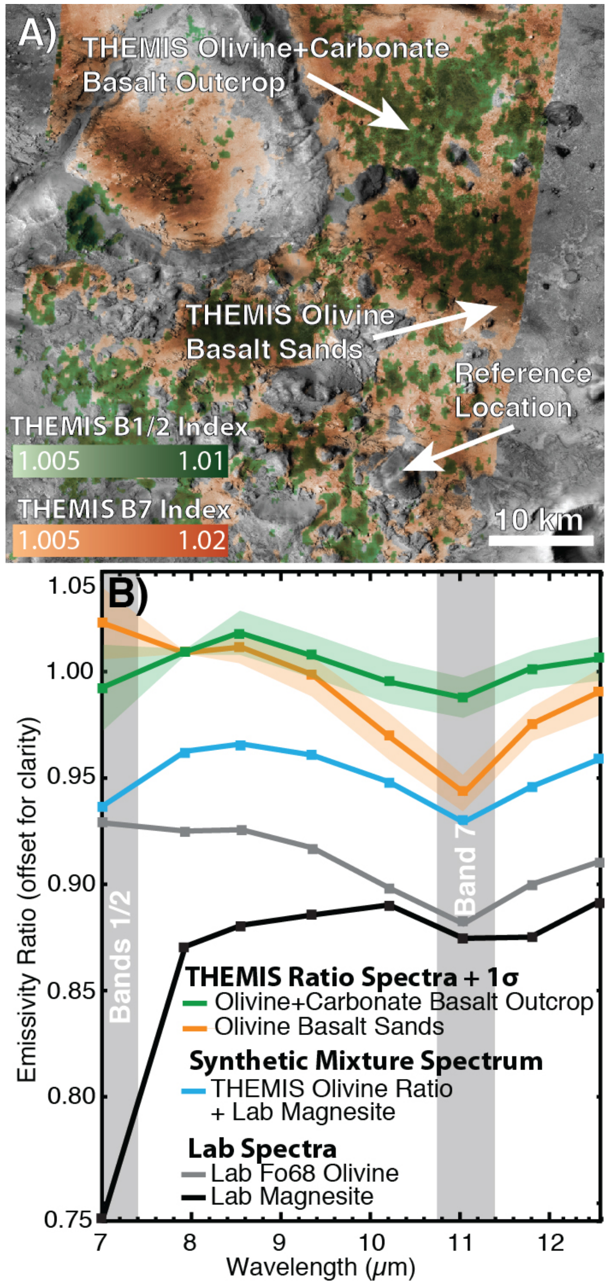

Figure 4. A: THEMIS carbonate (band 1+2 downturn) and olivine (band 7 band depth) indices (I36276032). B: THEMIS ratio and laboratory spectra of the Fe-Mg carbonate solid solution. Ratio spectra are from ~0.5 × 0.5 km areas on the olivine/carbonate-bearing basalt outcrops (green) and olivine-bearing basalt sands (orange) with 1-σ deviations on the average. The spectra of a synthetic mixture (cyan) of THEMIS olivine

Geology, 2015, doi: 10.1130/G36983.1
Accepted, Pre-Copy Edit version

sand ratio and laboratory carbonate (magnesite, black) spectra matches that of THEMIS spectrum of the carbonate-bearing, olivine basalt outcrops.

SUPPLEMENTARY MATERIALS

1.1 TES Data Analysis: Index Mapping and Deconvolution

TES data in this work were mapped using the Glotch and Rogers (2013) spectral index, which highlights long-wavelength spectral features due to Fe/Mg-carbonates and their decomposition products, in order to discriminate potential carbonate-bearing localities to perform TES quantitative analysis. Data for mapping and quantitative analysis were limited to locations with well-calibrated, clear atmosphere and warm surface temperatures (>250K, 9μm dust extinction <0.17, 11μm ice extinction <0.04, TES Lambert albedo <0.18, emission angles <5˚, no solar panel or mirror motion, and orbit counter keeper (OCK) values <7000). Mineral abundance determination and atmospheric correction was performed by modeling each TES emissivity spectrum with a library of mineral spectra (Table S3) and atmospheric components (Bandfield et al., 2000), using non-negative linear least-squares fitting (Rogers and Aharonson, 2008; Smith et al., 2000). This atmospheric/surface separation technique and endmember mineral deconvolution is commonly employed to determine mineral abundances to ~5-10% absolute areal abundance for minerals above the typical ~10% detection limit (Table S1) (Feely and Christensen, 1999; Ramsey and Christensen, 1998).

1.2 CRISM Data Analysis: Selection and Non-Linear Mixing

CRISM I/F data were atmospherically corrected using the volcano scan method (Murchie et al., 2009) and processed into spectral index parameters (Pelkey et al., 2007) to map the spatial distribution of carbonate (BD2300 & BD2500 (Ehlmann et al., 2008)) and olivine (OLINDEX2 (Salvatore et al., 2010)) and to identify locations with the strongest absorptions from which spectra were then extracted (Fig. 2). A single CRISM image (FRT0000C968) was processed through the Discrete Ordinate Radiative Transfer (DISORT) atmospheric retrieval algorithm, solving for carbon dioxide, water vapor, carbon monoxide, and associated Rayleigh scattering and discrete gas absorptions for CO_2, H_2O, and CO (Arvidson et al., 2014; Stamnes et al., 1988; Wiseman et al., 2012). These data were processed to single scattering albedo (SSA) to enable numerical modeling of the spectra by two methods (Ehlmann et al., 2011b): (1) a Hapke -style (Hapke, 1993) radiative transfer unmixing model that uses the optical constants of phases of interest (Table S4) to simultaneously solve for phase abundance and grain size by downhill simplex minimization of error between measured and modeled spectra over the 1.20 to 2.56 μm wavelength range; and (2) a forward model that uses laboratory-derived optical constants for magnesite with a scene-derived olivine-basalt spectrum to establish a relationship between band depth, single scattering albedo, and abundance for given mixing ratios and grain sizes of olivine-basalt and carbonate. Approach 2 assumes that the major compositional difference between the olivine-basalt bedrock and the carbonate-bearing materials is the addition of carbonate, an assumption warranted by TES and approach 1 results, discussed further herein. Note that in Approach 2, band depth at 2.3 μm, band depth at 2.5 μm, and SSA each bound the maximum possible carbonate. They must also produce simultaneously consistent values. Thus, while the albedo of the deposit permits up to 25 wt.% Mg-carbonate mixed with basalt, the observed depth of the 2.5-μm absorption in carbonate suggests the upper bound to be about 5 wt.%.

1.3 THEMIS Data Analysis: Composition and Thermophysics

Spectral ratios are commonly used when analyzing CRISM data but are rarely calculated with THEMIS data. Spectral ratios do not require fully atmospherically

Geology, 2015, doi: 10.1130/G36983.1
Accepted, Pre-Copy Edit version

corrected THEMIS images, which is advantageous in this region because coincident THEMIS and TES data that meet the requirements for a high quality correction are limited (Bandfield et al., 2004). All other THEMIS standard processing procedures were followed (Edwards et al., 2011). Due to the low signal-to-noise ratios (SNR) of bands 1 & 2 (6.78µm), originally designed to map carbonates (Christensen et al., 2004), our use of THEMIS spectral data is limited to spectral ratios and not quantitative unmixing; THEMIS is used primarily to highlight spectral differences between terrains. Two spectral indices, band 1/2 downturn and band 7 band depth, were developed to map olivine and carbonate-related spectral parameters over the region.

THEMIS thermal inertia data were also modeled over the entire region (Fergason et al., 2006). Thermal inertia data are sensitive to small changes in particle size (Piqueux and Christensen, 2011; Presley and Christensen, 1997) and are exceptionally sensitive to small volumes of pore filling cements (Piqueux and Christensen, 2009). We use these data in conjunction with spectral data to identify and map distinct compositional and thermophysical groupings.

Geology, 2015, doi: 10.1130/G36983.1
Accepted, Pre-Copy Edit version

SUPPLEMENTARY FIGURE CAPTIONS

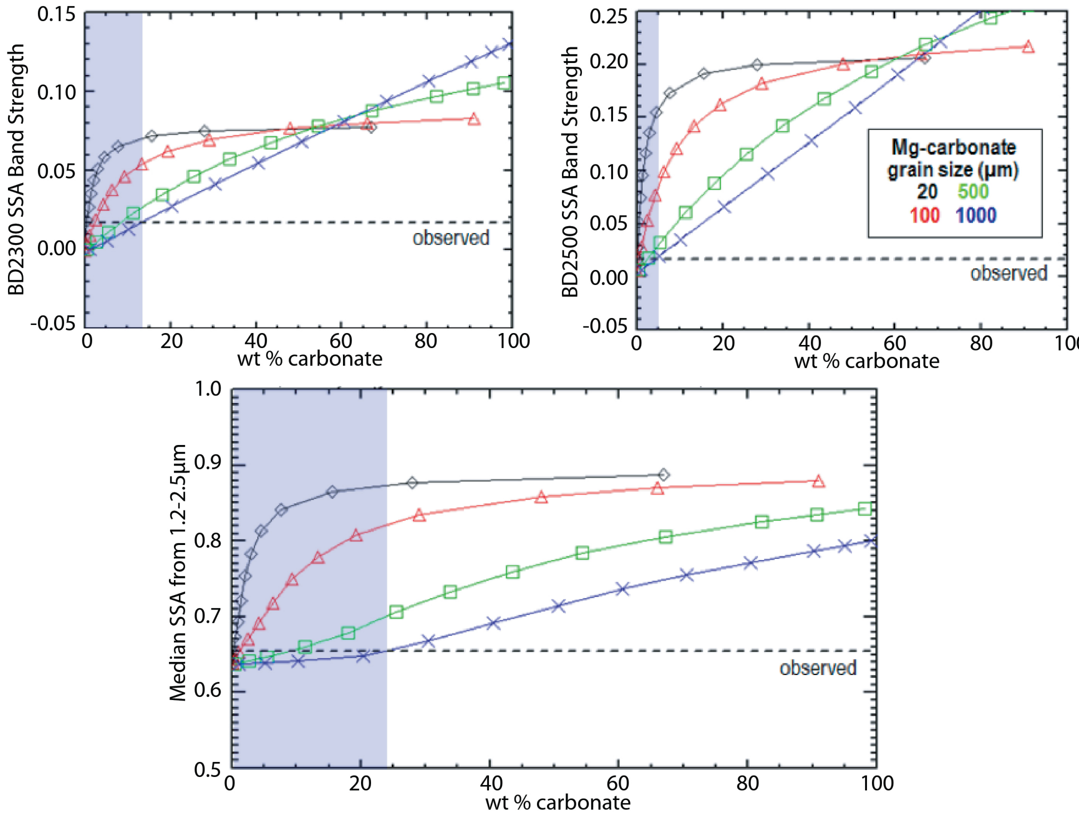

Figure DR1. Modeled infrared single scattering albedo (SSA), band depth at 2300 nm (BD2300), and band depth at 2500 nm (BD2500) for mixtures of carbonate with the olivine-enriched rock at Nili Fossae. Forward modeling was performed to generate simulated mixture spectra. The derived SSA olivine rock endmember spectrum from the CRISM scene was mixed with the SSA spectrum of magnesium carbonate from our optical constant library at different abundances. Grain size of the olivine-bearing rocks was assumed to be 1mm, based on Hapke inverse modeling results and THEMIS thermal inertia. The carbonate grain size was varied. All runs with the three parameters indicate carbonate abundances are lower than 25%. Observed BD2500 suggests abundances ≤5%.

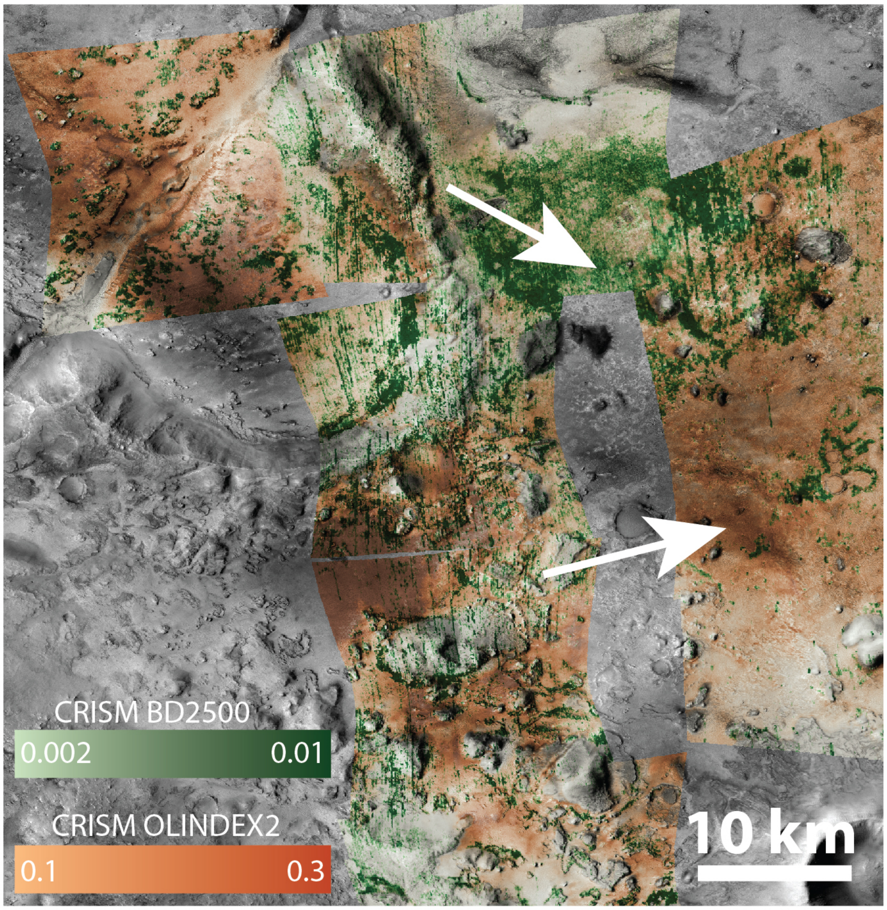

Figure DR2. CRISM BD2500 and OLINDEX2 band parameter maps over the same region as Fig. 4a. Linear streaks are artifacts in the image and not associated with surface features.

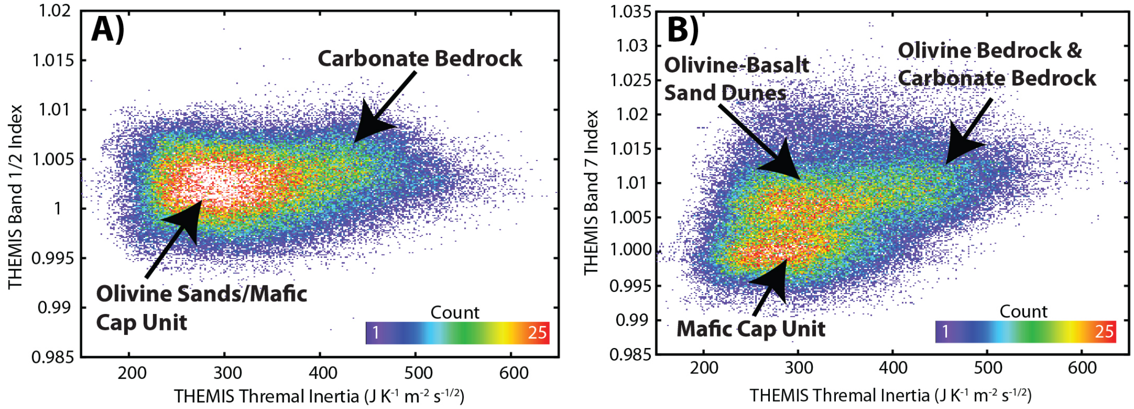

Figure DR3. Density plots of THEMIS band indices (Fig. 4a) for A: band 1 & 2 index and B: band 7. THEMIS TI over the region shown. Only the locations where both datasets were present are plotted.

Geology, 2015, doi: 10.1130/G36983.1
Accepted, Pre-Copy Edit version

SUPPLEMENTARY TABLES

Table DR1: TES model mineral abundances (%), Values reported in parentheses are ±1σ for derived abundances.

Mineral	TES[A&B]	TES[C]	Syrtis Type[b]
Pyroxene	21 (8)	27 (7)	32 (3)
Olivine	21 (4)	4 (5)	5 (3)
High-Si Phases	24 (8)	20 (7)	19 (10)
Carbonate	15 (4)	10 (1)	7 (1)
Feldspar	11 (7)	30 (10)	27 (6)
Other[a]	8 (3)	9 (3)	10 (2)
RMS Fit Error	0.35	0.35	0.14

[a]Values reported in the "Other" category include phases like hematite, sulfate, and quartz.
[b]Values from *Rogers and Christensen* (2007) of nearby Hesperian basalt for comparison

Table DR2: CRISM Derived abundances (wt % & grain size)

Phase	Carbonate Bedrock	Dark Bedrock	Dunes	Capping Unit
Carbonate	15 (1 mm)	1 (12μm)	8 (1mm)	1[#] (23μm)
Olivine	24 (~1mm)	26 (~1mm)	25 (~1mm)	5 (384μm)
Basalt	59 (950μm)	70 (560 μm)	65 (770μm)	89 (394μm)
Other*	2	2	2	5
RMS Fit Error	0.0038	0.0023	0.0033	0.0023
TI-Derived Grain Size^	$\gtrsim$1 mm	$\gtrsim$1 mm	$\gtrsim$1 mm	~300–700 μm

*Values reported in the "Other" category include phases like dust, additional feldspar & nontronite.
[#]Ill-fit; carbonate and nontronite introduce an absorption not present in the data. A hydrated phase not in our optical constant libraries is needed to account for the overall continuum shape.
^Grain Sizes

Geology, 2015, doi: 10.1130/G36983.1
Accepted, Pre-Copy Edit version

Table DR3: Library Mineral Endmembers for Linear Spectral Mixture Analysis of TES Data[a]

Mineral	**Group**
Quartz BUR-4120	*Quartz*
Microcline BUR-3460	*Feldspar*
Albite WAR-0235	*Feldspar*
Oligoclase BUR-060D	*Feldspar*
Andesine WAR-0024	*Feldspar*
Labradorite BUR-3080A	*Feldspar*
Bytownite WAR-1384	*Feldspar*
Anorthite BUR-340	*Feldspar*
Shocked An 17 GPa[b]	*Feldspar*
Shocked An 21 GPa[b]	*Feldspar*
Shocked An 25.5 GPa[b]	*Feldspar*
Shocked An 27 GPa[b]	*Feldspar*
Shocked An 38.2 GPa[b]	*Feldspar*
Shocked An 56.3 GPa[b]	*Feldspar*
Bronzite NMNH-93527	*Pyroxene*
Enstatite HS-9.4B	*Pyroxene*
Hypersthene NMNH-B18247	*Pyroxene*
Pigeonite[c]	*Pyroxene*
Diopside	*Pyroxene*
Augite NMNH-9780[c]	*Pyroxene*
Augite NMNH-122302[c]	*Pyroxene*
Hedenbergite DSM-HED01	*Pyroxene*
Forsterite BUR-3720A	*Olivine*
Fayalite WAR-RGFAY01	*Olivine*
Olivine Fo60 KI3362[d]	*Olivine*
Olivine Fo68 KI3115[d]	*Olivine*
Olivine Fo35 KI3373[d]	*Olivine*
Olivine Fo10 KI3008[d]	*Olivine*
Illite IMt-1	*High-Si Phase*
Montmorillonite STx-1	*High-Si Phase*
Saponite SpNv-1	*High-Si Phase*
Montmorillonite SWy-1	*High-Si Phase*
K-rich glass[e]	*High-Si Phase*
SiO2 glass[e]	*High-Si Phase*
Opal-A 02-011[f]	*High-Si Phase*
Aluminous opal[g]	*High-Si Phase*
Heulandite[h]	*High-Si Phase*
Stilbite[h]	*High-Si Phase*
Avg. Martian hematite[i]	*Hematite*
Anhydrite S9	*Sulfate*

Gypsum S6	*Sulfate*
Kieserite	*Sulfate*
Calcite C40	*Carbonate*
Dolomite C20	*Carbonate*
Magnesite MAGBB-1[j]	*Carbonate*
Siderite SIDIG-1[j]	*Carbonate*

a) All samples are from the ASU spectral library available at http://speclib.asu.edu Christensen et al. (2000) unless otherwise noted
b) Johnson et al. (2002)
c) Provided by V. E. Hamilton, described by Hamilton (2000)
d) Described by Koeppen and Hamilton (2008)
e) Described by Wyatt et al. (2001)
f) Described by Michalski et al. (2003)
g) Provided by M. D. Kraft
h) Described by Ruff (2004)
i) Derived from TES data, described by Glotch et al. (2004)
j) Described by Glotch and Rogers (2013)

432

Table DR4: Optical constants used for Hapke spectral unmixing of CRISM data. A variety of runs with greater and fewer constants (max of 7 per run) were executed with fitting over the wavelength range 1200-2560 nm. Those used in the final best-fit presented in the paper are indicated in the main text. The cap unit cannot be well-modeled with the same set as the olivine-bearing materials to produce an acceptable fit, pointing to a substantially different composition. Specifically, the continuum shape requires a hydrated phase, but inclusion of carbonate and nontronite leads to absorptions in modeled data that are not present in the actual data. The basaltic cap spectrum remained relatively ill-fit (Fig. 2) at the longest wavelengths (3-µm downturn) due to lack of an appropriate library optical constant match of the hydrated phase.

Phase	References
Olivine	*Ehlmann et al. (2011a; 2011b)*
Magnesite	*Ehlmann et al. (2011a; 2011b)*
Basalt	*Ehlmann et al. (2011a; 2011b)*
Feldspar (w/ magnetite inclusions)	*Poulet et al. (2008)*
Pyroxene	*Poulet et al. (2008)*
Dust	*Wolff et al. (2009)*
Nontronite (NG-1)	*Ehlmann et al. (2011a; 2001b)*

433

SUPPLEMENTARY REFERNCES

Arvidson, RE, et al., 2014, Ancient aqueous environments at Endeavour crater, Mars: Science, v. 343, no. 6169, p. 1248097

Bandfield, JL, et al., 2004, Atmospheric correction and surface spectral unit mapping using Thermal Emission Imaging System data: J. Geophys. Res., v. 109, p. E10008

Bandfield, JL, Smith, MD, and Christensen, PR, 2000, Spectral dataset factor analysis and endmember recovery: Application to analysis of martian atmospheric particulates: J. Geophys. Res., v. 105, p. 9573-9588

Christensen, PR, et al., 2000, A thermal emission spectral library of rock-forming minerals: Journal of Geophysical Research, v. 105, no. E4, p. 9735-9739

Christensen, PR, et al., 2004, The Thermal Emission Imaging System (THEMIS) for the Mars 2001 Odyssey Mission: Space Science Reviews, v. 110, no. 1, p. 85-130

Edwards, CS, et al., 2011, Mosaicking of global planetary image datasets: 1. Techniques and data processing for Thermal Emission Imaging System (THEMIS) multi-spectral data: J. Geophys. Res., v. 116, no. E10, p. E10008

Ehlmann, BL, et al., 2011a, CRISM-derived mineral abundances at the MSL landing sites: The Fifth Mars Science Laboratory Landing Site Workshop, p. May 16-18, Monrovia, Ca

Ehlmann, B, et al., 2011b, Estimating Modal Mineralogy of Mixtures with Phyllosilicates Using Radiative Transfer Modeling of Visible/Near Infrared Spectra, *in* Proceedings Lunar and Planetary Institute Science Conference Abstracts, Volume 42, p. 1704.

Ehlmann, BL, et al., 2008, Orbital identification of carbonate-bearing rocks on Mars: Science, v. 322, no. 5909, p. 1828

Feely, KC, and Christensen, PR, 1999, Quantitative compositional analysis using thermal emission spectroscopy: Application to igneous and metamorphic rocks: J. Geophys. Res., v. 104, p. 24,195-124,210

Fergason, RL, Christensen, PR, and Kieffer, HH, 2006, High resolution thermal inertia derived from THEMIS: Thermal model and applications: J. Geophys. Res., v. 111, p. E12004

Glotch, TD, et al., 2004, Effect of precursor mineralogy on the thermal infrared emission spectra of hematite: Application to martian hematite mineralization: J. Geophys. Res., v. 109, p. E07003

Glotch, TD, and Rogers, AD, 2013, Evidence for magma-carbonate interaction beneath Syrtis Major, Mars: J. Geophys. Res, v. 118, no. 1, p. 126-137

Hamilton, VE, 2000, Thermal infrared emission spectroscopy of the pyroxene mineral series: J Geophys Res-Planet, v. 105, no. E4, p. 9701-9716

Hapke, B, 1993, Combined Theory of Reflectance and Emittance Spectroscopy, *in* Pieters, CM, and Englert, PAJ, eds., Remote Geochemical Analysis: Elemental and Mineralogical Composition: Cambridge, Cambridge University Press

Johnson, JR, et al., 2002, Thermal infrared spectroscopy of experimentally shocked anorthosite and pyroxentie: Implications for remote sensing of Mars: J. Geophys. Res., v. 107(E10), p. 5073

Geology, 2015, doi: 10.1130/G36983.1
Accepted, Pre-Copy Edit version

Koeppen, WC, and Hamilton, VE, 2008, Global distribution, composition, and abundance of olivine on the surface of Mars from thermal infrared data: J. Geophys. Res, v. 113, p. E05001

Michalski, JR, et al., 2003, Thermal emission spectroscopy of the silica polymorphs and considerations for remote sensing of Mars: Geophys. Res. Lett., v. 30, no. 19, p. 2008

Murchie, SL, et al., 2009, Compact Reconnaissance Imaging Spectrometer for Mars investigation and data set from the Mars Reconnaissance Orbiter's primary science phase: J. Geophys. Res., v. 114

Pelkey, SM, et al., 2007, CRISM multispectral summary products: Parameterizing mineral diversity on Mars from reflectance: J. Geophys. Res, v. 112, p. E08S14

Piqueux, S, and Christensen, PR, 2009, A model of thermal conductivity for planetary soils: 2. Theory for cemented soils: J. Geophys. Res., v. 114, no. E09006

Piqueux, S, and Christensen, PR, 2011, Temperature-dependent thermal inertia of homogeneous Martian regolith: J. Geophys. Res., v. 116, p. E07004

Poulet, F, et al., 2008, Abundance of minerals in the phyllosilicate-rich units on Mars: Astronomy & Astrophysics, v. 487, no. 2, p. L41-U193

Presley, MA, and Christensen, PR, 1997, Thermal conductivity measurements of particulate materials, Part I: A review: J. Geophys. Res., v. 102, no. E3, p. 6535-6549

Ramsey, MS, and Christensen, PR, 1998, Mineral abundance determination: Quantitative deconvolution of thermal emission spectra: J. Geophys. Res., v. 103, p. 577-596

Rogers, AD, and Aharonson, O, 2008, Mineralogical composition of sands in Meridiani Planum determined from Mars Exploration Rover data and comparison to orbital measurements: J. Geophys. Res., v. 113, p. E06S14

Rogers, AD, and Christensen, PR, 2007, Surface mineralogy of martian low-albedo regions from MGS TES data: Implications for crustal evolution and surface alteration: J. Geophys. Res., v. 112, p. E01003

Ruff, SW, 2004, Spectral evidence for zeolite in the dust on Mars: Icarus, v. 168, no. 1, p. 131-143

Salvatore, MR, et al., 2010, Definitive evidence of Hesperian basalt in Acidalia and Chryse planitiae: J. Geophys. Res., v. 115, p. E07005

Smith, MD, Bandfield, JL, and Christensen, PR, 2000, Separation of atmospheric and surface spectral features in Mars Global Surveyor Thermal Emission Spectrometer (TES) spectra: Models and atmospheric properties: J. Geophys. Res., v. 105, no. E4, p. 9589-9608

Stamnes, K, et al., 1988, Numerically stable algorithm for discrete-ordinate-method radiative transfer in multiple scattering and emitting layered media: Appl Opt, v. 27, no. 12, p. 2502-2509

Wiseman, S, et al., Retrieval of atmospherically corrected CRISM spectra using radiative transfer modeling, *in* Proceedings Lunar and Planetary Institute Science Conference Abstracts2012, Volume 43, p. 2146.

Wolff, MJ, et al., 2009, Wavelength dependence of dust aerosol single scattering albedo as observed by the Compact Reconnaissance Imaging Spectrometer: J Geophys Res-Planet, v. 114, no. E2

Wyatt, MB, et al., 2001, Analysis of terrestrial and martian volcanic compositions using thermal emission spectroscopy: I. Determination of mineralogy, chemistry, and classification strategies: J. Geophys. Res., v. 106, no. E7, p. 14,711-714,732